

Article

Crystal-Plane Dependence of Nb-Doped Rutile TiO₂ Single Crystals on Photoelectrochemical Water Splitting

Tomohiko Nakajima * , Takako Nakamura and Tetsuo Tsuchiya

Advanced Coating Technology Research Center, National Institute of Advanced Industrial Science and Technology, Tsukuba Central 5, 1-1-1 Higashi, Tsukuba, Ibaraki 305-8565, Japan

* Correspondence: t-nakajima@aist.go.jp

Received: 29 July 2019; Accepted: 23 August 2019; Published: 28 August 2019



Abstract: The crystal-plane dependence of the photoelectrochemical (PEC) water-splitting property of rutile-structured Nb-doped TiO₂ (TiO₂:Nb) single-crystal substrates was investigated. Among the crystal planes, the (001) plane was a very promising surface for attaining good photocurrent. Under 1 sun illumination at 1.5 V vs. a reversible hydrogen electrode, the TiO₂:Nb(001) single-crystal substrate showed the highest photocurrent (0.47 mA/cm²) among the investigated substrates. The doped Nb ions were segregated inward from the top surface, and the TiO₂ ultrathin layer was formed at the surface of the crystal, resulting in the formation of a heterointerface between the TiO₂ and the TiO₂:Nb. The enhancement of the PEC properties of the TiO₂:Nb(001) single-crystal substrate originated from favorable atomic configurations for water molecule absorption and facilitation of transport of photoexcited electron–hole pairs in the depletion layer formed around the heterointerface of TiO₂ thin layers on the base crystal.

Keywords: photoelectrochemical water splitting; heterointerface; crystal-plane dependence

1. Introduction

Photoelectrochemical (PEC) reactions have been widely studied, especially for solar hydrogen production and water purification [1–5]. To improve the performance of PEC cells, the development of photoelectrodes with high activity under an excitation light is critical. Photoelectrodes for PEC reactions are usually composed of semiconductor layers and conducting bottom electrodes. Several key factors favor the improvement of photoelectrodes: (1) A large optical absorption and active surface area [6,7], (2) the effective adsorption of reactants onto the photoelectrode surface [8,9], (3) good excited charge separation [10], and (4) efficient excited charge transfer to the bottom electrodes [11–13]. Among these key factors, we focused on the properties of the crystal surface to attain new insights into the surface adsorption of reactants and photocarrier transport properties. In the case of crystal-plane surface dependence, numerous reports on crystal-facet-growth nanomaterials have appeared in the literature, and the role of each crystal plane in PEC reactions has been discussed [14–17].

In the present study, we investigated the PEC reaction of Nb-doped rutile TiO₂ (TiO₂:Nb) single-crystal substrates with (001), (100), (110), (101), and (111) crystal surfaces to clearly reveal the crystal-plane dependence of the photoelectrodes. TiO₂:Nb has been reported as a conductive material that exhibits photocatalytic and PEC reaction properties [18–21]. For such TiO₂:Nb crystals, we first revealed the formation of a heterointerface between the TiO₂ ultrathin layer and the Nb-doped base single crystal via segregation of doped Nb ions inward from the top surface; we then investigated the potential significance of the (001) surface plane of the TiO₂:Nb crystals on their PEC properties.

2. Results and Discussion

2.1. Surface Analysis

Figure 1 shows the schematic crystal structures of different crystal lattice plane surfaces of rutile $\text{TiO}_2\text{:Nb}$ [22]. The polished surfaces of the as-purchased single-crystal substrates were very flat; their surface roughness (R_a) was evaluated to be ca. 0.17–0.65 nm within a 150 nm square, as shown in the atomic force microscopy (AFM) images in Figure 2. Because the $\text{TiO}_2\text{:Nb}$ single-crystal substrates could not be annealed at high temperatures to preserve their conductivity as a bottom electrode, their surface morphology was not optimized to an atomic step-terrace structure. However, the crystals were cut parallel to each crystal plane within 0.5° accuracy, and we confirmed that the R_a values were sufficiently low.

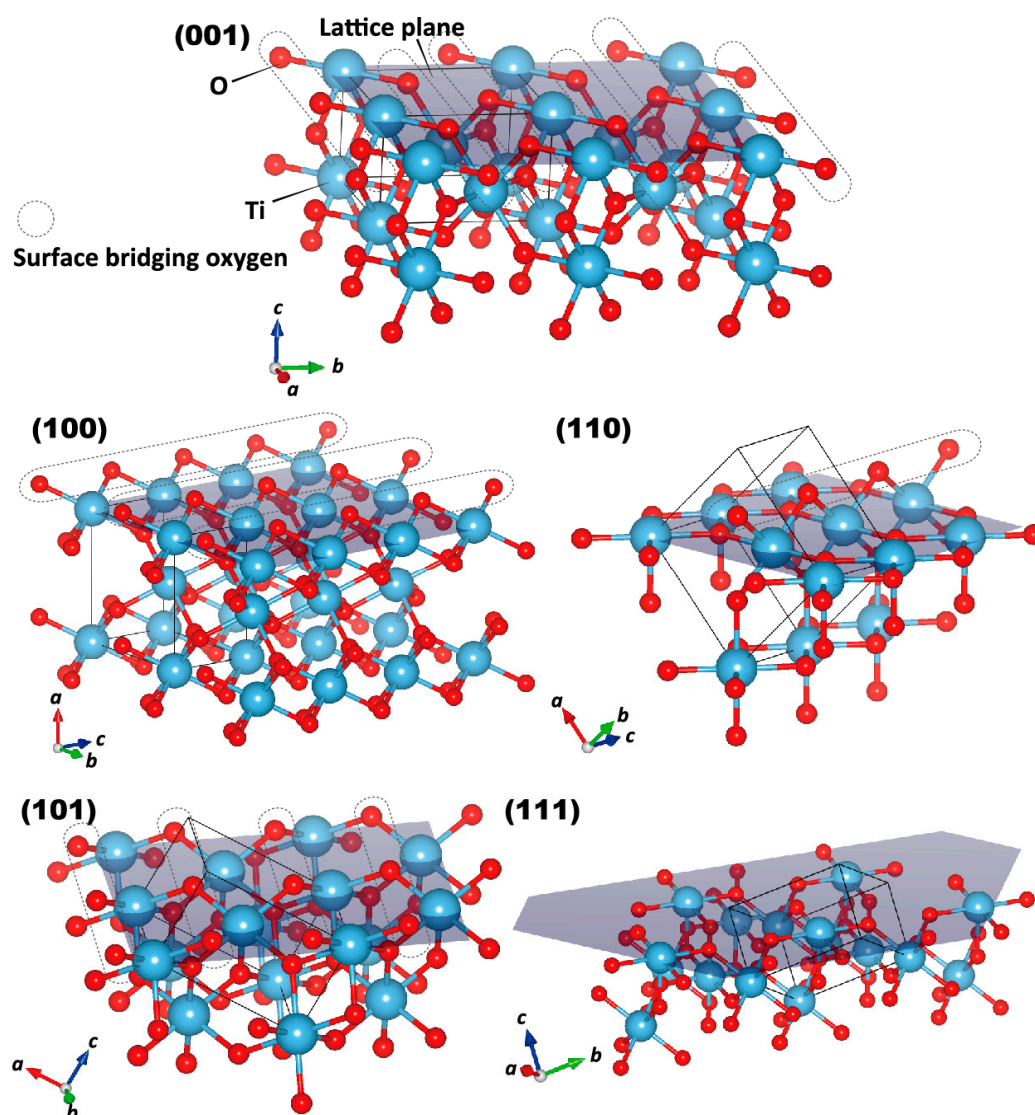


Figure 1. Schematic crystal structures for the (001), (100), (110), (101), and (111) planes of $\text{TiO}_2\text{:Nb}$. The light-blue and red spheres represent titanium and oxygen atoms, respectively. Some of the titanium atoms have been substituted by niobium atoms (0.43 at%). The gray planes and dotted ovals represent the crystal surface and bridging oxygen atoms, respectively.

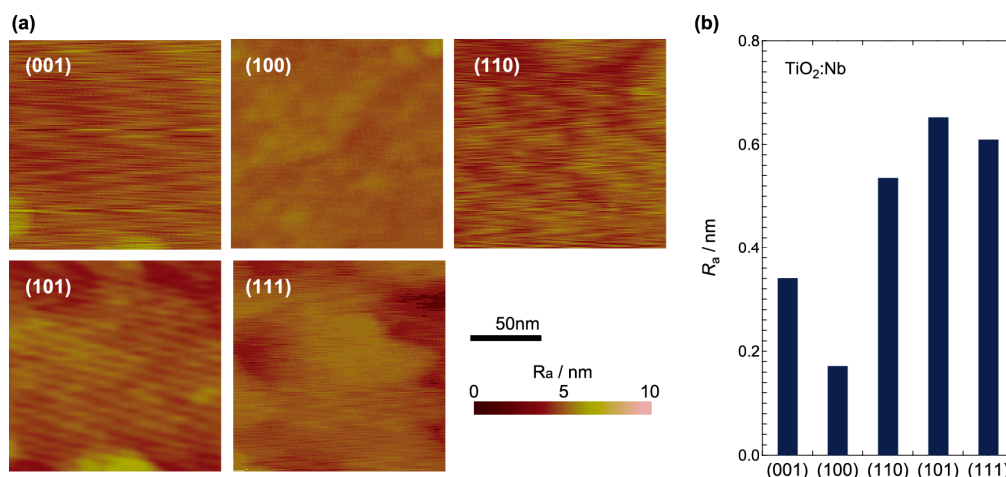


Figure 2. (a) AFM images and (b) surface roughness (R_a) values for the TiO₂:Nb single-crystal substrates.

Figure 3 shows the X-ray photoelectron spectroscopy (XPS) spectra of the Ti 2*p*, Nb 3*d*, and O 1*s* core levels for the TiO₂:Nb single-crystal substrates and reference materials (a pure TiO₂(001) single-crystal substrate and a TiO₂:Nb₂O₅ (0.43 at% Nb) polycrystalline powder composite). The observed Ti 2*p* core-level spectra of both TiO₂:Nb single-crystal substrates show two peaks at 458.5 (Ti 2*p*_{3/2}) and 464.4 eV (Ti 2*p*_{1/2}) (Figure 3a). These peak positions are approximately coincident with those of the pure TiO₂ and TiO₂:Nb₂O₅ composite references with Ti⁴⁺ ions in their lattice [23–25]. The observed Ti 2*p*_{3/2} and Ti 2*p*_{1/2} peaks in the spectra of the TiO₂:Nb single crystals were not shifted to the lower-energy side and broadened compared with the peaks in the spectrum of the TiO₂ reference. These results indicate that the Ti ions at the top surface of the TiO₂:Nb single crystals were not trivalent ions resulting from the Nb⁵⁺ doping in the lattice, but were rather tetravalent ions remaining from undoped TiO₂. The Nb 3*d* spectra of the TiO₂:Nb similarly support the tetravalent state of surface Ti ions (Figure 3b). The two typical Nb 3*d* peaks (3*d*_{3/2} and 3*d*_{5/2}) corresponding to the Nb⁵⁺ ions were very small in the spectra of the TiO₂:Nb single-crystal substrate surfaces, although these peaks were observed in the spectrum of the TiO₂:Nb₂O₅ (0.43 at% Nb) polycrystalline powder reference. With respect to the relative intensity ratio between the Nb 3*d*_{3/2} and Ti 2*p*_{3/2} and the calculated Nb content for each sample, the Nb signal in the spectra of the TiO₂:Nb single-crystal substrates was obviously small compared with that in the spectra of the TiO₂:Nb₂O₅ powder reference (Figure 4a). XPS analysis is a highly surface-sensitive technique and usually analyzes within a depth 0–10 nm from the top surface. For the whole single crystals of TiO₂:Nb, the doped Nb amount was evaluated to be 0.43 at% by X-ray fluorescence analysis. Therefore, we considered that the doped Nb ions at the top surface diffused inside the crystal in association with the valence conversion from Ti³⁺ to Ti⁴⁺ for Ti ions around the Nb ions because of surface oxidation immediately after the cutting and polishing of the surface of the substrates. This diffusion resulted in the formation of a gradual heteroepitaxial interface between the ultrathin TiO₂ layer (<10 nm) and the TiO₂:Nb at the top surface of the TiO₂:Nb single crystals.

Figure 3c shows the O 1*s* core-level XPS spectra of the TiO₂:Nb single crystals and the references. The main peak corresponding to the Ti–O bond was confirmed at 529.8 eV in the spectrum of each sample. Additionally, a broad peak was also observed at approximately 532.3 eV, which can be deconvoluted to two peaks at 531.7 eV and 532.5 eV attributed to Ti–OH bonding and physisorbed water molecules, respectively [23,24,26,27]. The Ti–OH hydroxyl groups on the rutile TiO₂ surface make the energy level 0.7 eV below the valence band of the TiO₂. This OH group on the surface was energetically stable and could not be oxidized easily by the valence-band holes. Thus, the surface OH groups could be easily stimulated for surface adsorption, functioning as reaction sites. As shown in Figure 4b, the intensity ratio of the Ti–OH to Ti–O peaks in the XPS spectra of the single-crystal substrates was much larger than that in the spectra of the powder reference.

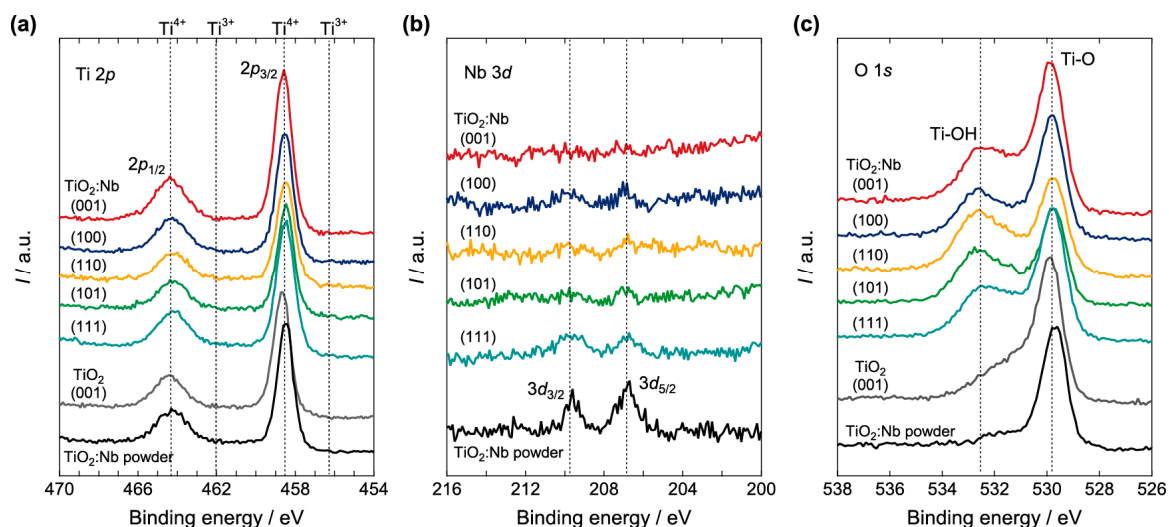


Figure 3. XPS spectra for (a) Ti 2p, (b) Nb 3d, and (c) O 1s core levels in the TiO₂:Nb (TiO₂) single-crystal substrates and TiO₂:Nb₂O₅ polycrystalline powder.

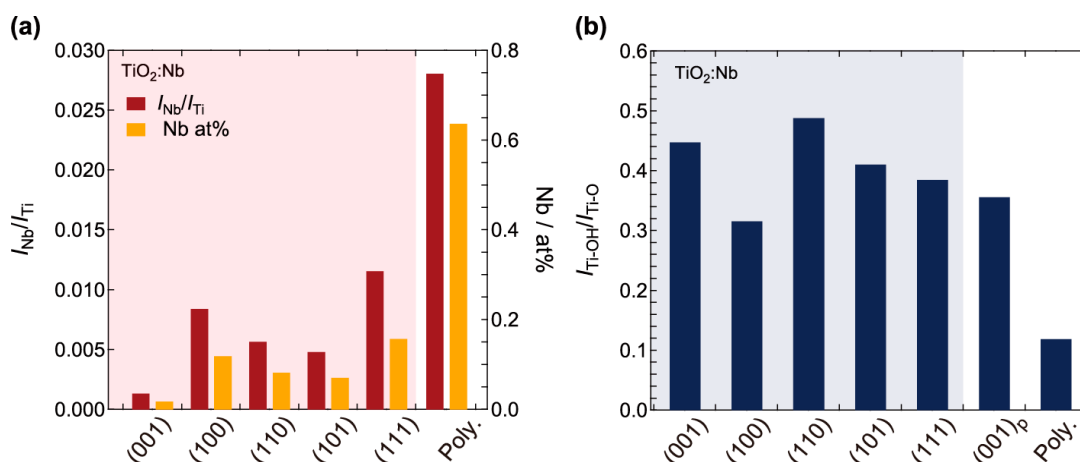


Figure 4. (a) Relative peak intensity ratio in the XPS spectra for Nb 3d_{3/2} and Ti 2p_{1/2} and the calculated Nb content (at%). (b) Relative peak intensity ratio in the XPS spectra for Ti–OH and Ti–O at the O 1s in the TiO₂:Nb (TiO₂) single-crystal substrates and TiO₂:Nb₂O₅ polycrystalline powder.

2.2. Photoelectrochemical and Optical Properties

Linear-sweep voltammetry (LSV) in aqueous 1 M KOH electrolyte under 1 sun illumination was carried out to evaluate the PEC properties of the TiO₂:Nb single-crystal substrates with (001), (100), (110), (101), and (111) surface planes for water splitting (Figure 5a). The TiO₂:Nb(001) substrate showed the largest photocurrent density (J) among the investigated substrates. The open-circuit potential (OCP) under 1 sun illumination was 0.08 V vs. a reversible hydrogen electrode (V_{RHE}). The J increased with increasing applied bias voltage and became saturated at 0.47 mA/cm² at approximately 0.6 V_{RHE} (Figure 5b). Although the TiO₂:Nb(001) photoanode was very flat without any modification of the surface structure to increase its active surface area, the photocurrent would have been very high. For example, this photocurrent value of single crystal TiO₂:Nb(001) reached around a half of the value reported in the well-organized Nb-doped TiO₂ nanotube arrays [28]. This observation suggests that the Nb-doped TiO₂ single crystal and the heterostructure with the very thin rutile TiO₂(001) top layer functioned well for PEC water oxidation. The η_{max} for this very flat TiO₂(001)/TiO₂:Nb(001) photoanode was 0.3% at 0.47 V_{RHE} . The PEC performance of the TiO₂:Nb substrates was strongly dependent on the crystal planes of the surface. The TiO₂:Nb(100) and (110) substrates showed a 20–25% smaller maximum J and 0.10–0.13 V_{RHE} higher OCP than those of TiO₂:Nb(001). The TiO₂:Nb(101)

exhibited a similar OCP value as the $\text{TiO}_2\text{:Nb}(001)$; however, the maximum J remained 75% of that of the $\text{TiO}_2\text{:Nb}(001)$. Among the photoresponses of the investigated substrates, the photoresponse of the $\text{TiO}_2\text{:Nb}(111)$ substrate, in particular, differed from that of the $\text{TiO}_2\text{:Nb}(001)$ substrate. Although the photocurrent started to increase very gradually from $0.08 V_{\text{RHE}}$, it was not saturated by $1.5 V_{\text{RHE}}$. The η_{max} for $\text{TiO}_2\text{:Nb}(111)$ decreased to 0.05% because of a lack of a steep rise in the photocurrent.

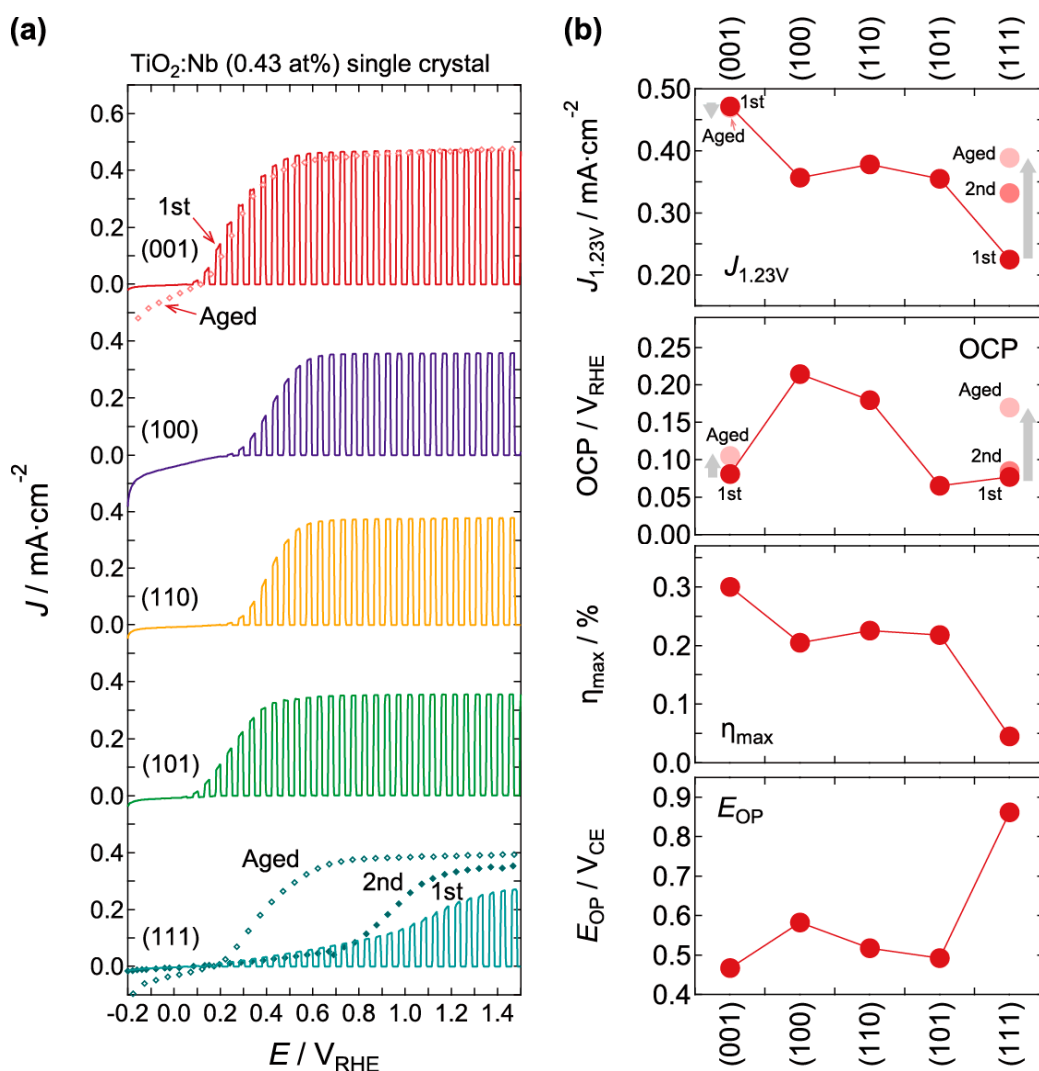


Figure 5. (a) The LSV curves for the $\text{TiO}_2\text{:Nb}(001)$, (100), (110), (101), and (111) single-crystal substrates. The “1st” and “2nd” simply represent the frequency of LSV measurement for the fresh substrate. The data which do not show the annotation mean measurements for the fresh substrates. The “aged” represent the sample after the PEC reaction at $1.5 V_{\text{RHE}}$ for 30 min. (b) The surface plane dependence of $\text{TiO}_2\text{:Nb}$ substrates on J at $1.23 V_{\text{RHE}}$ ($J_{1.23\text{V}}$), OCP, η_{max} , and effective bias potential for the η_{max} (E_{OP}).

The variations in the PEC properties of the crystal faces in the $\text{TiO}_2\text{:Nb}$ single-crystal photoanodes were likely caused by (1) surface absorption of water molecules, (2) surface recombination of photoexcited electron–hole pairs, and (3) electron transfer at the heterojunction interfaces between the thin semiconducting TiO_2 layer and the metal $\text{TiO}_2\text{:Nb}$ base crystal. The surface absorption ability of water molecules in rutile-structured TiO_2 crystals has been discussed from the viewpoint of the atomic configurations of Ti and O at the surface. For the (001) direction of TiO_2 crystals, the oxygen ions are aligned densely (Figure 1); in addition, the four-fold-coordinated Ti atoms at the (001) plane surface, which are surrounded by bridging oxygen atoms, were evaluated by first-principle calculations to be displaced inside the lattice [29]. As a result of the formation of a high charge density induced

by the bridging oxygen ion layer at the top surface, the PEC water oxidation reaction could be enhanced [30–33]. At the (100) and (110) planes of a TiO_2 crystal, the density of Ti ions is relatively higher than at the (001), (101), and (111) planes. The nearest-neighbor Ti–Ti distances for the (100), (110), (001), (101), and (111) planes are 0.296 nm, 0.296 nm, 0.459 nm, 0.357 nm, and 0.546 nm, respectively [22]. The low-coordinate Ti ions at the top surface tend to be electron trapping sites that are unfavorable for the oxidation reaction. Therefore, the (100) and (110) planes of $\text{TiO}_2\text{:Nb}$ substrates could show higher OCP values than the other crystallographic planes. Thus, we considered that the variation of the PEC properties at the $\text{TiO}_2/\text{TiO}_2\text{:Nb}$ heterojunction would be strongly dependent on the surface affinity of each crystallographic plane for the water molecules. On the basis of this factor, the strange behavior of the LSV curve corresponding to the (111) plane can be also explained. The (111) plane of TiO_2 exhibits a relatively low density of Ti ions and is mainly covered by oxygen ions. Therefore, a high electron density would be favorable for the oxidation reaction, resulting in a higher OCP value. However, the (111) surface only has the five-fold-coordinated Ti atoms that do not elaborate the bridging oxygen atoms at the surface; this surface exhibits low adsorption ability for the water molecules. Consequently, the adsorption of water molecules as the rate-limiting reaction would cause a gradual increase of the photocurrent for the applied bias voltage.

Thus, we concluded that the (001) plane of $\text{TiO}_2\text{:Nb}$ crystals was very effective on the PEC oxidation reaction for the water splitting, and the oxidized TiO_2 layer on the $\text{TiO}_2\text{:Nb}(001)$ produced the large photocurrent regardless of the very thin thickness. The enhancement of photocurrent would have been strongly related to the surface absorption ability associated with the crystallographic features. On the contrary, the (111) plane of $\text{TiO}_2\text{:Nb}$, in addition to its poor PEC performance, had difficulty utilizing the surface for the PEC reaction. As shown in Figure 5, the PEC behavior of the $\text{TiO}_2\text{:Nb}(111)$ surface varied greatly during the measurements. In the second run of the LSV measurement, the photocurrent growth behavior already differed from the first run. After the PEC reaction at 1.5 V_{RHE} for 1 h (aged sample), the LSV curve showed a clear saturation at approximately 0.8 V_{RHE} .

Figure 6 shows the field-emission scanning electron microscopy (FESEM) images for the surface morphology of $\text{TiO}_2\text{:Nb}(001)$ and (111) substrates before and after the PEC reaction. The top-surface morphology of both fresh substrates was very flat, without any nanostructuring. However, the surface of $\text{TiO}_2\text{:Nb}(111)$ after the PEC reaction clearly showed a nanoflake array structure as a result of photo-etching. Although a large etching structure was not observed on the $\text{TiO}_2\text{:Nb}(001)$ after the PEC reaction, the surface exhibited a slight granular modulation. For the TiO_2 crystals, the top surface can be photo-etched along the $\langle 001 \rangle$ direction to make (100) etched pit walls and a (001) basal plane [34,35], and the etching rate under acidic electrolyte conditions is much higher than that under the alkaline condition [36]. In the present study, we carried out the PEC measurements in a strongly alkaline electrolyte (1 M KOH). Nevertheless, strong etching was observed on the $\text{TiO}_2\text{:Nb}(111)$ surface. This etching could be due to the low density of Ti and O ions at the top surface, where only basal planes of isolated pyramidal TiO_5 appeared. Therefore, the alkaline (acidic) medium can easily attack the isolated Ti ions at the surface, enabling the penetration of etchant into the crystals. For the other crystal planes, we confirmed that very deep etching as the (111) plane was not observed (Figure S1).

We next evaluated the surface plane dependence of the PEC property for the $\text{TiO}_2\text{:Nb}$ single-crystal substrates on the basis of their optical properties. Figure 7a shows the optical absorption spectrum for each substrate. All of the substrates exhibited large optical absorption of the incident light with wavelengths ranging from the UV to the visible region (300–650 nm). Whereas the absorption of $\text{TiO}_2\text{:Nb}(001)$ was slightly larger (ca. 2–3%) than the absorptions of the other crystal planes over the whole spectral range, the spectral shapes were very similar: The absorption was 70–74% in the visible range (450–650 nm) and decreased to 54–58% with decreasing wavelength. We carried out photon-to-current conversion efficiency (IPCE) measurements at 1.5 V_{RHE} for evaluating the optical absorption effect on the PEC reaction (Figure 7b). The IPCE spectra of the $\text{TiO}_2\text{:Nb}$ substrates at 1.5 V_{RHE} showed 2.4–2.9% absorption at 300 nm that decreased to 0.1% at approximately 410 nm. With increasing wavelength, the IPCE spectra showed a very weak absorption maximum of approximately 0.2% at

505 nm that decreased at wavelengths longer than 580 nm. At the weak maximum (505 nm), the IPCE values for all of the substrates with different crystal planes were very similar to each other. On the contrary, IPCE spectral changes were clearly observed in the UV range rather than in the visible range, whereas the TiO₂:Nb exhibited large absorption of visible light by the Nb doped into the TiO₂ lattice. The TiO₂:Nb(001) exhibited the highest value among them, and the IPCE at 300 nm reached 2.9%. The J variation calculated by the integral of photocurrent collected from the IPCE measurements in the range of 300–700 nm (Table 1 and Figure S2) were almost consistent with the observed J (Figure 5a), while the calculated one for the (111) plane was relatively higher than the observed value.

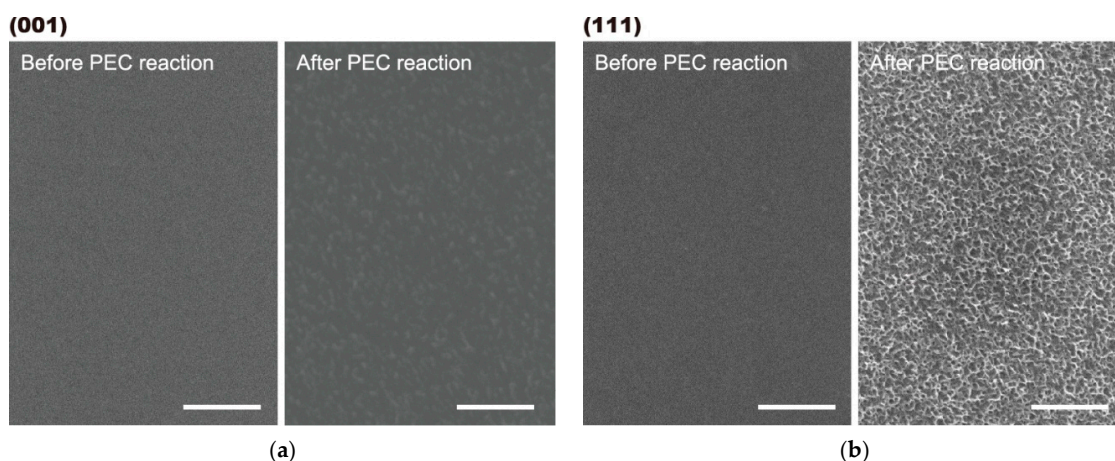


Figure 6. The surface morphology for the (a) (001)- and (b) (111)-planes of TiO₂:Nb substrates before and after the PEC reaction at 1.5 V_{RHE} for 1 h in 1 M KOH electrolyte. The white scale bars represent 500 nm.

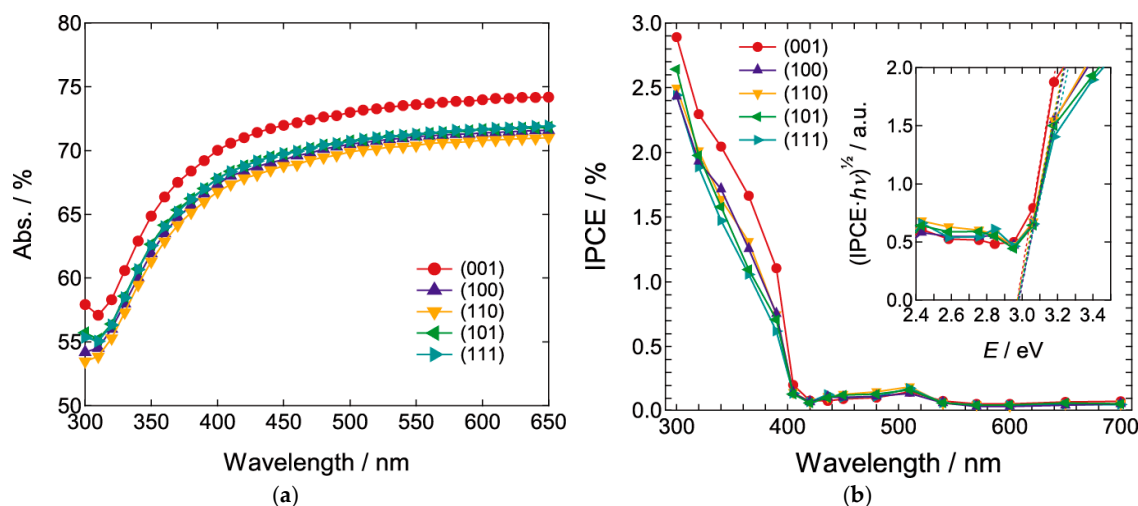


Figure 7. (a) Optical absorption and (b) IPCE spectra for the TiO₂:Nb(001), (100), (110), (101), and (111) single-crystal substrates. The IPCE data were recorded at 1.5 V_{RHE} in 1 M KOH electrolyte under monochromatic light illumination.

Table 1. Observed J at 0.55 V_{RHE} ($J_{0.55V}$) and calculated J value from the IPCE spectra.

Lattice Plane	$J_{0.55V}/\text{mA}/\text{cm}^2$	$J_{\text{IPCE}}/\text{mA}/\text{cm}^2$
(001)	0.444	0.393
(100)	0.314	0.316
(110)	0.342	0.345
(101)	0.339	0.329
(111)	0.057	0.290

The aforementioned results indicate that the PEC property was not directly enhanced by the large absorption of visible light by the Nb-doped TiO₂ crystals. Enhancement of the PEC property was also observed in the hydrogenated and cation/anion-doped TiO₂, especially at the UV range, though the samples also exhibited large optical absorption for visible light [37]. Wang et al. explained this behavior in hydrogenated TiO₂ as follows [38]: The hydrogenation of TiO₂ increases the electron donor density, resulting in the Fermi level shifting to the conduction band of TiO₂. This approach promotes charge separation and transport of photoexcited electron–hole pairs, leading to enhancement of the PEC reaction. The electronic transition between the vacancy level and the delocalized conduction band does not show a substantial contribution to the PEC reaction because of the weak coupling of localized/delocalized energy states. Therefore, the electron–hole pairs photoexcited by the higher photon energy (UV range) associated with the major optical absorption band of TiO₂ are considered to mainly contribute to the PEC reaction, which should be enhanced by the electronically-activated transport property derived from the doping/defects in the TiO₂ lattice. Our results were also supported by this mechanism. In our case, there are two possible explanations for the excitation and transport process: (1) The stimulation of photoexcited charge separation and transport at the heterointerface between the very thin TiO₂ layer and the TiO₂:Nb base crystal may enhance the PEC property; and (2) the enhancement of charge separation and transport by doping mainly occurs at the interface between the TiO₂/TiO₂:Nb and electrolyte.

The charge recombination inhibition scenario would actually work effectively in the TiO₂/TiO₂:Nb system, although the extent of both contributions is not easy to distinguish because of the ultra-thinness of the TiO₂ layer on the base crystal. Figure 8a shows the photoluminescence (PL) spectra for TiO₂:Nb single-crystal substrates. The photoluminescence (PL) intensity is generally correlated with the recombination of photoexcited electron–hole pairs, and the intensity variation of TiO₂:Nb substrates was strongly related to the photocurrent response behavior. The exact onset potential of the TiO₂:Nb(111) was difficult to evaluate correctly because of the very gradual increase of its photocurrent. Therefore, we evaluated the onset potential as a bias voltage at 10% increase from the dark current for the photocurrent at 1.23 V_{RHE}. The PL intensity for each substrate was linked to the onset potential value. This result means the cathodic shift of the photocurrent rise behavior was obviously associated with the inhibition of photoexcited recombination, which was dependent on the crystal surface planes (Figure 8b).

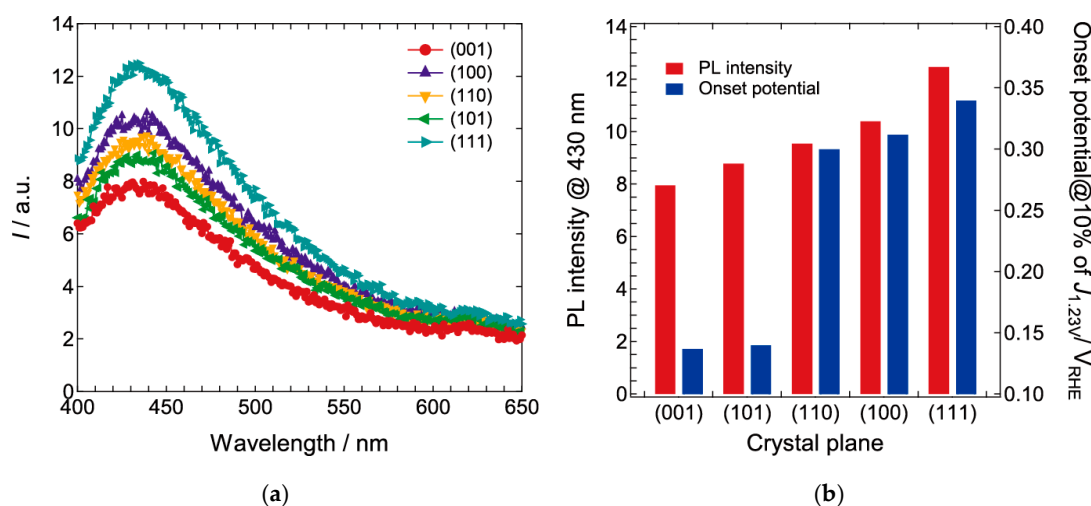


Figure 8. (a) PL spectra for the TiO₂:Nb substrates excited at 350 nm. (b) The PL intensity at 430 nm and onset potential defined as the bias voltage at 10% of the photocurrent at 1.23 V_{RHE} for each substrate.

2.3. Electrical Impedance Spectral Analysis of the Transport Property

We carried out electrical impedance spectroscopy (EIS) for the $\text{TiO}_2\text{:Nb}$ single-crystal substrates to evaluate the surface plane dependence of their reaction and transport kinetics. The electrical analog for the electrolyte, TiO_2 thin layer, and the $\text{TiO}_2\text{:Nb}$ base crystal is shown in Figure 9. The surface TiO_2 thin layer is semiconducting, and it forms an interface with the electrolyte. Therefore, the electrical circuit can be expressed by a series resistance (R_s) and two RC elements for the semiconducting layer (R_{sc} and space charge capacitance, C_{sc}) and the semiconducting layer and electrolyte interface (R_{ct} and Helmholtz capacitance, C_H). For the capacitances of this model, we employed a constant phase element (CPE).

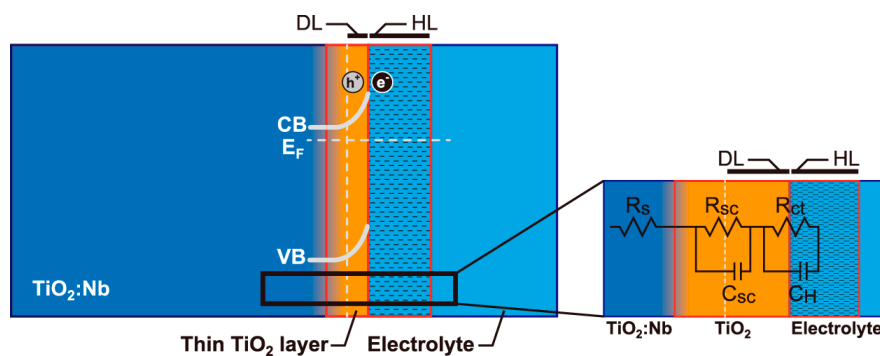


Figure 9. Energy diagram and electrical circuit analog for the $\text{TiO}_2/\text{TiO}_2\text{:Nb}$. The CB, VB, E_F , DL and HL represent the conduction band, valence band, Fermi energy, depletion layer and Helmholtz layer, respectively.

The EIS measurements were carried out for the $\text{TiO}_2\text{:Nb}$ substrates under dark conditions in a three-electrode setup at $1.5 V_{\text{RHE}}$ (Figure 10). Two semicircles were observed in the Nyquist diagrams of both samples, corresponding to the RC elements for the semiconductor layer and the interface between the semiconductor layer and the electrolyte. The fitted parameters based on the equivalent electrical circuit, as shown in Figure 9, are listed in Table 2. Although the resistance value R_s for the base crystal and the parameters associated with the charge transfer phenomena at the interface between the semiconductor layer and the electrolyte (R_{ct} and C_H) appeared to not be directly linked to the PEC property, a correlation between the PEC property and the parameters for the depletion layer, R_{sc} , and C_{sc} was found. The C_{sc} of the (001) plane of $\text{TiO}_2\text{:Nb}$ was especially lower than the others, indicating the efficient reaction of minority carriers in the depletion layer. This efficient reaction could be related to the structural features of the (001) plane. The Ti ions along to the $\langle 001 \rangle$ direction are connected via bridging oxygens, whereas the Ti ions link in an oblique direction in the other crystal planes. The structural advantage for transport along the $\langle 001 \rangle$ direction can stimulate carrier transport.

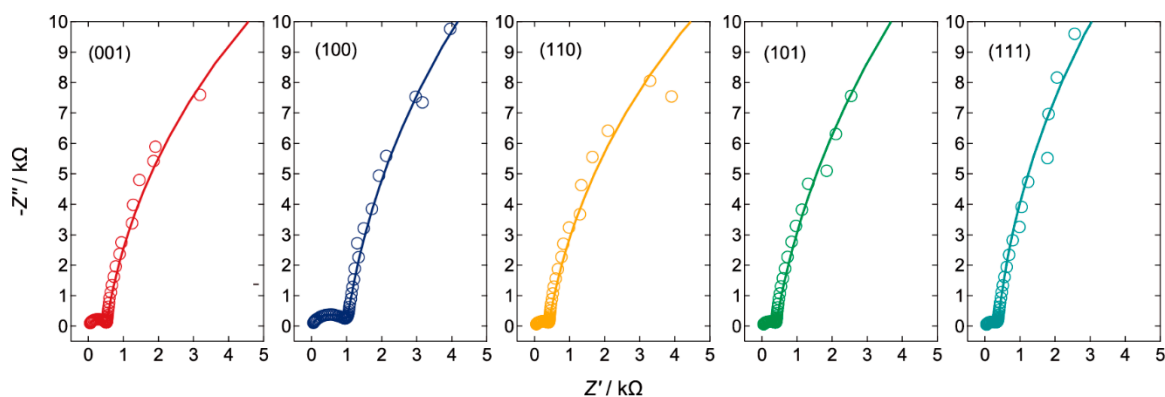


Figure 10. The Nyquist diagrams of $\text{TiO}_2\text{:Nb}$ single-crystal substrates with the (001), (100), (110), (101), and (111) crystal-plane surface measured at $1.5 V_{\text{RHE}}$ under 1 sun illumination.

Table 2. Fitted parameters of the Nyquist plots for single-crystal TiO₂:Nb photoanodes.

LATTICE PLANE	R_s/Ω	R_{sc}/Ω	CPE _{sc}		$R_{ct}/k\Omega$	CPE _H	
			C_{sc}/nFs^{n-1}	n		$C_H/\mu Fs^{n-1}$	n
(001)	15.7	496.3	51.9	0.914	42.3	3.34	0.918
(100)	11.8	853.4	242	0.785	55.9	3.81	0.926
(110)	17.2	385.7	363	0.800	44.0	4.34	0.912
(101)	16.5	377.2	355	0.802	60.5	4.35	0.908
(111)	9.66	368.0	783	0.751	58.7	2.84	0.947

We also evaluated the other crystal planes from the EIS results. In the (100) plane of TiO₂:Nb, the transient transport property presumed by the C_{sc} was relatively better than that in the (110) and (101) planes; however, the bulk resistance R_{sc} was more than twice that of the (110) and (101) planes. In the (111) plane, the C_{sc} was very high compared with the other values, which would cause slow dynamics of charge transfer. On the basis of these results, the EIS parameters did not play a critical role in the PEC property. However, only the (001) plane showed a clear advantage (very low C_{sc}) and did not have a large disadvantage with respect to photocarrier transport. The heteroepitaxial relationship between the TiO₂ layer and the TiO₂:Nb(001) was also considered to positively affect carrier transport. In addition to the aforementioned (001) surface structural features that favor the water oxidation reaction, the transportation enhancement in the depletion layer near the heterointerface between the TiO₂ thin layer and the base crystal was an important origin of the good PEC reaction on the TiO₂:Nb(001) substrate.

3. Materials and Methods

3.1. Materials

The 0.43 at% Nb-doped TiO₂ and pure TiO₂ crystals used in the experiments were commercial rutile-structured single-crystal substrates with five different surface orientations ((001), (100), (110), (101), and (111) for the Nb-doped TiO₂ and (001) for the TiO₂) (SHINKOSHA). The reference TiO₂:Nb₂O₅ (0.43 at% Nb) polycrystalline powder composite was synthesized by the solid-state reaction of TiO₂ (rutile) and Nb₂O₅ with 99.99% purities (rare metallic). Starting reagents were ground thoroughly, pressed into pellets, and then heated at 800 °C for 12 h in air.

3.2. Sample Characterization

AFM images were recorded with a Nanoscope IIIa (Digital Instruments, NY, USA) using a silicon cantilever in tapping mode. XPS measurements were performed using a PHI ESCA model 5800 system (ULVAC-PHI, Inc., Kanagawa, Japan) with monochromatic Al K α excitation (1486.6 eV) at 100 W with a pass energy of 23.50 eV and a step size of 0.1 eV. The intensity analyses were carried out using Ti 2p_{3/2} peaks as a reference. The signals were deconvoluted with Gaussian peak shapes. The surface morphology was determined by FESEM; Hitachi SU9000 (Tokyo, Japan). The optical absorbance spectra were recorded using a UV-visible spectrophotometer (UV-3150, Shimadzu, Kyoto, Japan). The PL spectra were evaluated with a C9920-02 spectrometer (Hamamatsu Photonics, Shizuoka, Japan) equipped with an Xe lamp, a monochromator, a back-illuminated multichannel charge-coupled device photodetector, and an integrating sphere.

3.3. PEC Performance Evaluation

Under 100 mW/cm² AM1.5 simulated sunlight (1 sun) from a 150 W Xe lamp, LSV for solar water-splitting photocurrent measurements was performed in 1.0 M KOH (pH = 13.6) at 0.0–1.5 V vs. a reversible hydrogen electrode (V_{RHE}) in a three-electrode electrochemical cell equipped with a quartz glass window. An Ag/AgCl reference electrode in saturated KCl solution and a Pt wire counter electrode were used, and the scan rate was 5 mV/s. The measured potential vs. Ag/AgCl ($V_{Ag/AgCl}$)

in the three-electrode system was converted to the V_{RHE} according to a following equation: $V_{\text{RHE}} = V_{\text{Ag/AgCl}} + 0.059 \text{ pH} + V_{\text{Ag/AgCl}}^0$, where $V_{\text{Ag/AgCl}}^0 = 0.1976$ at 25°C . The STH efficiency (η) of the photoanodes was measured using a two-electrode configuration cell with a Pt wire as the counter electrode. The following equation was used for estimating STH values: $\eta = J(1.23 - E_{\text{CE}})/I_{\text{AM1.5}}$, where J is the photocurrent density (mA/cm^2), E_{CE} is the applied bias voltage vs. the counter electrode, and $I_{\text{AM1.5}}$ is the irradiance of AM1.5 simulated sunlight at $100 \text{ mW}/\text{cm}^2$. The IPCE was evaluated using the three-electrode setup with the equation $\text{IPCE} = 1240 J/\lambda I$, where λ is the incident-light wavelength (nm) and I is the intensity of the light source at each wavelength (mW/cm^2). The bias voltage was $0.55 V_{\text{RHE}}$. The monochromatic light was generated using an Xe lamp with optical narrow-band filters. EIS measurements were performed on a PGSTAT302N potentiostat equipped with an impedance analyzer FRA32M (Metrohm Autolab, Herisau, Switzerland). The frequency range was from 0.01 Hz to 100 kHz, and the modulation signal was 10 mV. All measurements were conducted at $1.5 V_{\text{RHE}}$ under 1 sun illumination.

4. Conclusions

We showed the crystal-plane dependence of PEC water-splitting property for the rutile $\text{TiO}_2\text{:Nb}$ single-crystal substrates, and that the (001) crystal plane was the most promising surface for obtaining the good photocurrent. We revealed that the doped Nb ions were segregated from the top surface, and that the TiO_2 thin layer was formed at the surface of crystal, resulting in the formation of a heterointerface between the TiO_2 and $\text{TiO}_2\text{:Nb}$. The enhancement of PEC property in the $\text{TiO}_2\text{:Nb}(001)$ single-crystal substrate was originated from the favorable atomic configurations for the water molecule absorption and the facilitation of transportation of photoexcited electron/hole pairs in the depletion layer formed around the heterointerface of TiO_2 thin layer with the base crystal.

Supplementary Materials: The following are available online at <http://www.mdpi.com/2073-4344/9/9/725/s1>, Figure S1: The surface morphology for the (100)-, (110)- and (101)-planes of $\text{TiO}_2\text{:Nb}$ substrates after the PEC reaction at $1.5 V_{\text{RHE}}$ for 1 h in 1 M KOH electrolyte. The white scale bars represent 500 nm., Figure S2: The spectra for $100 \text{ mW}\cdot\text{cm}^{-2}$ AM1.5G (1 SUN) and simulated solar light used for the IPCE measurements.

Author Contributions: T.N. (Tomohiko Nakajima) conducted most of the experiments and analyses and wrote the manuscript. T.N. (Takako Nakamura) carried out the XPS analysis. All authors discussed the experimental results and interpretation.

Funding: This work was partly supported by a Grant-in-Aid for Young Scientists (B) No. 25820338 from the Japan Society for the Promotion of Science.

Acknowledgments: The authors thank N. Fukuda for the technical help.

Conflicts of Interest: The authors declare no conflicts of interest.

References

1. Alexander, B.D.; Kulesza, P.J.; Rutkowska, I.; Solarska, R.; Augustynski, J. Metal oxide photoanodes for solar hydrogen production. *J. Mater. Chem.* **2008**, *18*, 2298–2303. [[CrossRef](#)]
2. Nowotny, J.; Bak, T.; Nowotny, M.K.; Sheppard, L.R. Titanium dioxide for solar-hydrogen I. Functional properties. *Int. J. Hydrogen Energy* **2007**, *32*, 2609–2629. [[CrossRef](#)]
3. Kronawitter, C.X.; Vayssieres, L.; Shen, S.; Guo, L.; Wheeler, D.A.; Zhang, J.Z.; Antoun, B.R.; Mao, S.S. A perspective on solar-driven water splitting with all-oxide hetero-nanostructures. *Energy Environ. Sci.* **2011**, *4*, 3889–3899. [[CrossRef](#)]
4. Osterloh, F.E. Inorganic nanostructures for photoelectrochemical and photocatalytic water splitting. *Chem. Soc. Rev.* **2013**, *42*, 2294–2320. [[CrossRef](#)] [[PubMed](#)]
5. Nakajima, T.; Hagino, A.; Nakamura, T.; Tsuchiya, T.; Sayama, K. WO_3 nanosponge photoanodes with high applied bias photon-to-current efficiency for solar hydrogen and peroxydisulfate production. *J. Mater. Chem. A* **2016**, *4*, 17809–17818. [[CrossRef](#)]
6. Dang, H.X.; Hahn, N.T.; Park, H.S.; Bard, A.J.; Mullins, C.B. Nanostructured Ta_3N_5 films as visible-light active photoanodes for water oxidation. *J. Phys. Chem. C* **2012**, *116*, 19225–19232. [[CrossRef](#)]

7. Nakajima, T.; Lee, C.-Y.; Yang, Y.; Schmuki, P. N-Doped lepidocrocite nanotubular arrays: Hydrothermal formation from anodic TiO₂ nanotubes and enhanced visible light photoresponse. *J. Mater. Chem. A* **2013**, *1*, 1860–1866. [[CrossRef](#)]
8. Wang, Z.; Yang, C.; Lin, T.; Yin, H.; Chen, P.; Wan, D.; Xu, F.; Huang, F.; Lin, J.; Xie, X.; et al. Visible-light photocatalytic, solar thermal and photoelectrochemical properties of aluminium-reduced black titania. *Energy Environ. Sci.* **2013**, *6*, 3007–3014. [[CrossRef](#)]
9. Yi, Z.; Ye, J.; Kikugawa, N.; Kako, T.; Ouyang, S.; Stuart-Williams, H.; Yang, H.; Cao, J.; Luo, W.; Li, Z.; et al. An orthophosphate semiconductor with photooxidation properties under visible-light irradiation. *Nat. Mater.* **2010**, *9*, 559–564. [[CrossRef](#)]
10. Pan, X.; Yang, M.-Q.; Fu, X.; Zhang, N.; Xu, Y.-J. Defective TiO₂ with oxygen vacancies: Synthesis, properties and photocatalytic applications. *Nanoscale* **2013**, *5*, 3601–3614. [[CrossRef](#)]
11. Pinaud, B.A.; Vesborg, P.C.K.; Jaramillo, T.F. Effect of film morphology and thickness on charge transport in Ta₃N₅/Ta photoanodes for solar water splitting. *J. Phys. Chem. C* **2012**, *116*, 15918–15924. [[CrossRef](#)]
12. Seki, M.; Yamahara, H.; Tabata, H. Enhanced photocurrent in Rh-substituted α -Fe₂O₃ thin films grown by pulsed laser deposition. *Appl. Phys. Express* **2012**, *5*, 115801-1–115801-3. [[CrossRef](#)]
13. Nakajima, T.; Nakamura, T.; Tsuchiya, T. The significant effect of heterojunction quality on photoelectrochemical water splitting in bilayer photoelectrodes: Rb_xWO₃ thin films on RbLaNb₂O₇ layers. *Phys. Chem. Chem. Phys.* **2014**, *16*, 26901–26908. [[CrossRef](#)] [[PubMed](#)]
14. Mu, L.; Zhao, Y.; Li, A.; Wang, S.; Wang, Z.; Yang, J.; Wang, Y.; Liu, T.; Chen, R.; Zhu, J.; et al. Enhancing charge separation on high symmetry SrTiO₃ exposed with anisotropic facets for photocatalytic water splitting. *Energy Environ. Sci.* **2016**, *9*, 2463–2469. [[CrossRef](#)]
15. Li, W.; Bai, Y.; Liu, W.; Liu, C.; Yang, Z.; Feng, X.; Lu, X.; Chan, K.-Y. Single-crystalline and reactive facets exposed anatase TiO₂ nanofibers with enhanced photocatalytic properties. *J. Mater. Chem.* **2011**, *21*, 6718–6724. [[CrossRef](#)]
16. Ye, L.; Mao, J.; Liu, J.; Jiang, Z.; Peng, T.; Zan, L. Synthesis of anatase TiO₂ nanocrystals with {101}, {001} or {010} single facets of 90% level exposure and liquid phase photocatalytic reduction and oxidation activity orders. *J. Mater. Chem. A* **2013**, *1*, 10532–10537. [[CrossRef](#)]
17. Ballestas-Barrientos, A.; Li, X.; Yick, S.; Masters, A.F.; Maschmeyer, T. Optimised heterojunctions between [100]-oriented rutile TiO₂ arrays and {001} faceted anatase nanodomains for enhanced photoelectrochemical activity. *Sustain. Energy Fuels* **2018**, *2*, 1463–1473. [[CrossRef](#)]
18. Hitosugi, T.; Ueda, A.; Nakao, S.; Yamada, N.; Furubayashi, Y.; Hirose, Y.; Shimada, T.; Hasegawa, T. Fabrication of highly conductive Ti_{1-x}Nb_xO₂ polycrystalline films on glass substrates via crystallization of amorphous phase grown by pulsed laser deposition. *Appl. Phys. Lett.* **2007**, *90*, 212106-1–212106-3. [[CrossRef](#)]
19. Tucker, R.T.; Beckers, N.A.; Fleischauer, M.D.; Brett, M.J. Electron beam deposited Nb-doped TiO₂ toward nanostructured transparent conductive thin films. *Thin Solid Films* **2012**, *525*, 28–34. [[CrossRef](#)]
20. Trenczek-Zając, A.; Radecka, M.; Rekas, M. Photoelectrochemical properties of Nb-doped titanium dioxide. *Physica B Condens. Matter* **2007**, *399*, 55–59. [[CrossRef](#)]
21. Yang, M.; Jha, H.; Liu, N.; Schmuki, P. Increased photocurrent response in Nb-doped TiO₂ nanotubes. *J. Mater. Chem.* **2011**, *21*, 15205–15208. [[CrossRef](#)]
22. Baur, W.H.; Khan, A.A. Rutile-type compounds. VI. SiO₂, GeO₂ and a comparison with other rutile-type structures. *Acta Crystallogr. B* **1971**, *27*, 2133–2139. [[CrossRef](#)]
23. Philippin, G.; Delhalle, J.; Mekhalif, Z. Comparative study of the monolayers of CH₃-(CH₂)_n-SiCl₃ and CH₃-(CH₂)_n-PO(OH)₂, n = 4 and 13, adsorbed on polycrystalline titanium substrates. *Appl. Surf. Sci.* **2003**, *212–213*, 530–536. [[CrossRef](#)]
24. Kačulis, S.; Mattogno, G.; Napoli, A.; Bemporad, E.; Ferrari, F.; Montenero, A.; Gnappi, G. Surface analysis of biocompatible coatings on titanium. *J. Electron Spectrosc.* **1998**, *95*, 61–69. [[CrossRef](#)]
25. Nakajima, T.; Nakamura, T.; Shinoda, K.; Tsuchiya, T. Rapid formation of black titania photoanodes: Pulsed laser-induced oxygen release and enhanced solar water splitting efficiency. *J. Mater. Chem. A* **2014**, *2*, 6762–6771. [[CrossRef](#)]
26. Krishna, V.; Bai, W.; Han, Z.; Yano, A.; Thakur, A.; Georgieva, A.; Tolley, K.; Navarro, J.; Koopman, B.; Moudgil, B. Contaminant-activated visible light photocatalysis. *Sci. Rep.* **2018**, *8*, 1894-1–1894-11. [[CrossRef](#)]

27. Idriss, H. Surface reactions of uranium oxide powder, thin films and single crystals. *Surf. Sci. Rep.* **2010**, *65*, 67–109. [[CrossRef](#)]
28. Das, C.; Roy, P.; Yang, M.; Jha, H.; Schmuki, P. Nb doped TiO₂ nanotubes for enhanced photoelectrochemical water-splitting 2011, 3, 3094–3096. *Nanoscale* **2011**, *3*, 3094–3096. [[CrossRef](#)]
29. Ramamoorthy, M.; Vanderbilt, D.; King-Smith, R.D. First-principle calculations of the energetics of stoichiometric TiO₂ surfaces. *Phys. Rev. B* **1994**, *49*, 16721–16727. [[CrossRef](#)]
30. Lowekamp, J.B.; Rohrer, G.S.; Hotsenpiller, P.A.M.; Bolt, J.D.; Farneth, W.E. Anisotropic photochemical reactivity of bulk TiO₂ crystals. *J. Phys. Chem. B* **1998**, *102*, 7323–7327. [[CrossRef](#)]
31. Ohno, T.; Sarukawa, K.; Matsumura, M. Crystal faces of rutile and anatase TiO₂ particles and their roles in photocatalytic reactions. *New J. Chem.* **2002**, *26*, 1167–1170.
32. Haisch, C.; Günemann, C.; Melchers, S.; Fleisch, M.; Schneider, J.; Emeline, A.V.; Bahnemann, D.W. Irreversible surface changes upon n-type doping—A photoelectrochemical study on rutile single crystals. *Electrochim. Acta* **2018**, *280*, 278–289.
33. Fujishima, A.; Zhang, X.; Tryk, D.A. TiO₂ photocatalysis and related surface phenomena. *Surf. Sci. Rep.* **2008**, *63*, 515–582. [[CrossRef](#)]
34. Harris, L.A.; Wilson, R.H. Aging effects in single crystal reduced rutile anodes. *J. Electrochem. Soc.* **1976**, *123*, 1010–1015. [[CrossRef](#)]
35. Tsujiko, A.; Kisumi, T.; Magari, Y.; Murakoshi, K.; Nakato, Y. Selective formation of nanoholes with (100)-face walls by photoetching of *n*-TiO₂ (rutile) electrodes, accompanied by increases in water-oxidation photocurrent. *J. Phys. Chem. B* **2000**, *104*, 4873–4879. [[CrossRef](#)]
36. Imanishi, A.; Okamura, T.; Ohashi, N.; Nakamura, R.; Nakato, Y. Mechanism of water photooxidation reaction at atomically flat TiO₂ (rutile) (110) and (100) surfaces: Dependence on solution pH. *J. Am. Chem. Soc.* **2007**, *129*, 11569–11578. [[CrossRef](#)]
37. Hu, Y.H. A highly efficient photocatalyst—hydrogenated black TiO₂ for the photocatalytic splitting of water. *Angew. Chem. Int. Ed.* **2012**, *51*, 12410–12412. [[CrossRef](#)]
38. Wang, G.; Wang, H.; Ling, Y.; Tang, Y.; Yang, X.; Fitzmorris, R.C.; Wang, C.; Zhang, J.Z.; Li, Y. Hydrogen-treated TiO₂ nanowire arrays for photoelectrochemical water splitting. *Nano Lett.* **2011**, *11*, 3026–3033. [[CrossRef](#)]



© 2019 by the authors. Licensee MDPI, Basel, Switzerland. This article is an open access article distributed under the terms and conditions of the Creative Commons Attribution (CC BY) license (<http://creativecommons.org/licenses/by/4.0/>).